Showcasing research from the team of
Dr Sumanta Kumar Karan, Prof. Bed Poudel and
Prof. Shashank Priya at the Department of Materials
Science and Engineering, Pennsylvania State University,
University Park, PA, USA.

Magnetic field and ultrasound induced simultaneous
wireless energy harvesting

A novel dual energy harvesting technology using magnetic
field and ultrasound-driven wireless energy transfer has
been demonstrated to convert magnetic/acoustic energy
into electricity using magnetoelectric (ME) devices. The
millimeter scale ME device is capable of producing high
power (>50 mW) in water/porcine tissue operating under
safety limits, making it suitable for powering several IoT
devices including implantable and embedded devices.

Cover artwork by Kai Wang.

As featured in:

ROYAL SOCIETY
OF **CHEMISTRY**

rsc.li/ees

PAPER

Check for updates

Magnetic field and ultrasound induced simultaneous wireless energy harvesting†

Sumanta Kumar Karan, [iD] *[a] Sujay Hosur, [iD] [b] Zeinab Kashani,[b] Haoyang Leng, [iD] [a] Anitha Vijay,[c] Rammohan Sriramdas, [iD] [ad] Kai Wang,[a] Bed Poudel, [iD] [a] Andrew D. Patterson,[c] Mehdi Kiani*[b] and Shashank Priya*[a]

Energy harvesting can provide continuous power required for operating biomedical, physical, and chemical devices. However, providing sufficient power for many devices utilizing only a single modality through energy harvesting is still challenging due to its restricted power density considering the source energy that is below human body safety limits. Here, for the first time a high-power density energy harvester using piezoelectric and magnetoelectric conversion is demonstrated operating within the human body safety limit. This dual harvester can harvest energy from different directions, which makes it insensitive to the source orientation. Prototype design is demonstrated to harvest magnetic and ultrasound energies simultaneously from a single device traveling through liquid/tissue media generating an ultra-high power of $\sim$52.1 mW (a power density of $\sim$597 mW cm^{-3}) across input of $\sim$500 μT rms magnetic field and $\sim$675 mW cm^{-2} ultrasound intensity, which are below the safety limits prescribed by the IEEE and FDA. This represents an $\sim$225% improvement compared to individual magnetoelectric systems utilizing a single source under safety limits. The device can recharge a 3 V lithium-ion battery with 1 mA-h capacity at a rate of $\sim$1.67 mC s^{-1} in porcine tissue. These findings suggest that the dual energy harvester based on magnetic field and ultrasound intensity has the potential to power various electronic devices, such as implantable devices and embedded components.

Broader context

Energy harvesting is advantageous for powering low-power electronics, sensor networks, and Internet of Things (IoT) devices. Magnetic field (MF) and ultrasound (US) energy based devices have relevance for implantable medical devices (IMDs) due to wireless energy transfer. Power density using a single source such as MF or US is not enough for IMDs, since the magnitude of the input source has to be kept low in order to meet the human body safety limits. One of the ways to enhance the magnitude of output power is by increasing the surface area of the device; however, this is not a desired option for IMDs. Furthermore, previously reported energy harvesting devices have been designed to provide best performance from a single input source and thus do not exhibit any significant advantages from dual input sources. Here, a novel disk-shaped multi-mode energy harvester using magnetoelectric mechanism is demonstrated, which can provide higher output power ($\sim$52.1 mW) within human body safety limits while being insensitive to the source misalignment. It utilizes a dual wireless energy transfer strategy capturing the input MF and US at the same time. The harvester is shown to charge a 3 V, 1 mAh capacity Li-ion battery at a rate of $\sim$1.67 mC s^{-1} in porcine tissue under *ex vivo* conditions. The proposed dual energy transfer structure advances the next generation of power sources.

[a] Department of Materials Science and Engineering, The Pennsylvania State University, University Park, PA 16802, USA. E-mail: skk5867@psu.edu, sumanta.karan.fula@gmail.com, sup103@psu.edu

[b] School of Electrical Engineering and Computer Science, The Pennsylvania State University, University Park, PA 16802, USA. E-mail: muk42@psu.edu

[c] Department of Veterinary and Biomedical Sciences, The Pennsylvania State University, University Park, PA 16802, USA

[d] Department of Mechanical Engineering, Amrita School of Engineering, Coimbatore, Amrita Vishwa Vidyapeetham 641112, India

† Electronic supplementary information (ESI) available. See DOI: **https://doi.org/10.1039/d3ee03889k**

Introduction

Wireless energy harvesting technology has emerged as a promising solution to extend the lifetime of energy-constrained mobile electronics, implantable medical devices (IMDs), sensor networks and Internet of Things (IoT) devices.[1] The growth of IoT has led to the development of different types of wireless sensors that are used for monitoring, transduction, communication, and IMDs.[2–4] Wireless sensors and transceivers in a typical IoT device is currently powered by batteries.[5] Power requirements for wireless sensors vary from one application to

This journal is © The Royal Society of Chemistry 2024

Energy Environ. Sci., 2024, **17**, 2129–2144 | 2129

another, typically in the range of a few microwatts to several milliwatts.[6,7] Due to the large numbers of IoT devices that are deployed in difficult to access areas, regular battery replacement is practically impossible.[8] In all these scenarios, wireless power transfer combined with energy harvesting is a viable alternative for powering the devices. There are several mechanisms for converting ambient energy into electricity, including inductive, photovoltaic, thermoelectric, magneto-thermoelectric, electromagnetic, magneto-mechano-electric, piezoelectric, triboelectric, pyroelectric, and various other principles.[3,9–17] Wireless recharging technology for *in vitro* and *in vivo* applications has been widely investigated.[18,19] However, wireless power transfer using radio frequencies has been observed to experience attenuation as it passes through tissue, thereby restricting the amount of power that can be transmitted to a harvesting device. Exposure to high levels of transmitted radio power can cause tissue damage in humans during transmission. An inductive coupling system is highly dependent on the distance/alignment between the coils, and for it to operate efficiently, it must be operated at high frequencies (in the 100s of MHz range). The safety limits are particularly restricted at high frequencies, which results in limitations on the amount of power that can be transmitted.[20] The low frequency (in the kHz range) magneto-electric and ultrasound-based methods of energy harvesting offer higher efficiencies and power densities, making them promising alternatives.[21,22] Magnetic field (MF) energy harvesting using magnetoelectric devices involves two steps: AC magnetic field to mechanical strain (magnetostriction) and mechanical strain to electric potential (piezoelectricity).[12] Magnetoelectric transducers offer a promising solution for low-frequency magnetic field energy harvesting as they experience less absorption and heating and greater penetration through different tissue (lossy) media.[21] In the last decade, magneto-mechano-electric generators have gained attention for harvesting 50–60 Hz magnetic field energy using various materials such as PZT/Metglas, textured Fe–Ga/SCMF PMN–PZ–PT, Ni/low-loss PMN–PZ–PT, Ni/PMN–PZ–PT, *etc.*[12,23–25] Most of the reported devices have been designed to operate under strong magnetic fields (> 500 μT) and possess large dimensions due to low frequency resonance requirements. Small sized magnetoelectric energy harvesters have been explored using different piezoelectric materials for biomedical applications such as endovascular stimulation, multisite stimulation, neurostimulation, *etc.*[26–29] Demonstrated ME devices in the literature are not able to generate high enough power to charge the battery at a faster rate within a given size and human safety limits. As per the IEEE standard, for an operational frequency of ~ 250 kHz, the applied AC magnetic field strength ≤ 5.5 Oe rms (at an implant depth of 30 mm) and DC magnetic field strength ≤ 1670 Oe are considered to be safe.[30]

Alternatively, ultrasound (US) energy has low attenuation in biological tissue compared to that of electromagnetic waves, which not only reduces energy dissipation but also enables a deeper travel depth at a given power.[22,31–33] The energy transfer through ultrasound energy in biomedical applications has been demonstrated using piezoelectric transducers.[31] Non-invasive triboelectric nano-generators have been explored for signal communication,[26] transient electronics[34] and battery charging for pacemakers.[22] However, these systems either use heavy and bulky piezo/tribo transducers to harvest energy or have low output power with low power transfer efficiency within human safety limits. FDA regulations limit ultrasound intensity exposure on the human body to a maximum of 720 mW cm^{-2} for medical diagnostic purposes, as exceeding this threshold can result in tissue damage, abnormal cell migration, and neurodegenerative diseases.[35,36] Long-term power supply to implanted devices such as cochlear implants, spinal-cord stimulators, and pacemakers is a technological challenge, especially with the increasing demand for smaller size and higher power density devices. Individual magnetic field and ultrasound based technology has difficulty in obtaining the high-power capability within the human body safety limit and angular misalignment limit.

To overcome the above limitations and achieve required power density, new multi-mode energy harvesting technologies are required. Harvesting magnetic and ultrasound energies simultaneously provides a promising opportunity for meeting the goals of high-power density, compatibility with wireless power transfer over a certain distance, and packaging the device within given volumetric and weight constraints.

Here we demonstrate a novel hybrid energy harvesting technology using both the ultrasound and magnetic energies in water/tissue (*ex vivo*) media (Fig. 1a and b). The newly designed magnetoelectric device with disk architecture is comprised of a high energy density novel MnO_2 and CuO co-doped $Pb(In,Nb)O_3$–$Pb(Mg,Nb)O_3$–$PbTiO_3$ (PIN–PMN–PT) piezoelectric disk-shaped transducer sandwiched between magnetostrictive Metglas layers (discussed in detail in the ESI,† Note S1–S2, Fig. S1–S2 and Table S1). The magnetic field and ultrasound induced dual generator (MUDG) produces an ultrahigh rms power of ~ 52.1 mW with a power density of ~ 597 mW cm^{-3} at an ~ 500 μT magnetic field and 675 mW cm^{-2} ultrasound intensity. This is the highest reported value compared to those of all the previously reported devices with the applied input under safety limits (Fig. 1c). Results demonstrate that the MUDG can overcome the limitations of traditional wireless power transfer systems for human body application, providing a novel platform with the advantages of ultra-high-power density, small size, biocompatibility, and tolerance to angular misalignment (*xy*/*yz* plane). Systematic studies, including device performance optimization, the powering of electronics using harvester power, transcutaneous transmission (Fig. 1d), power transfer ex vivo, and biosafety analysis, were conducted to evaluate its full potential.
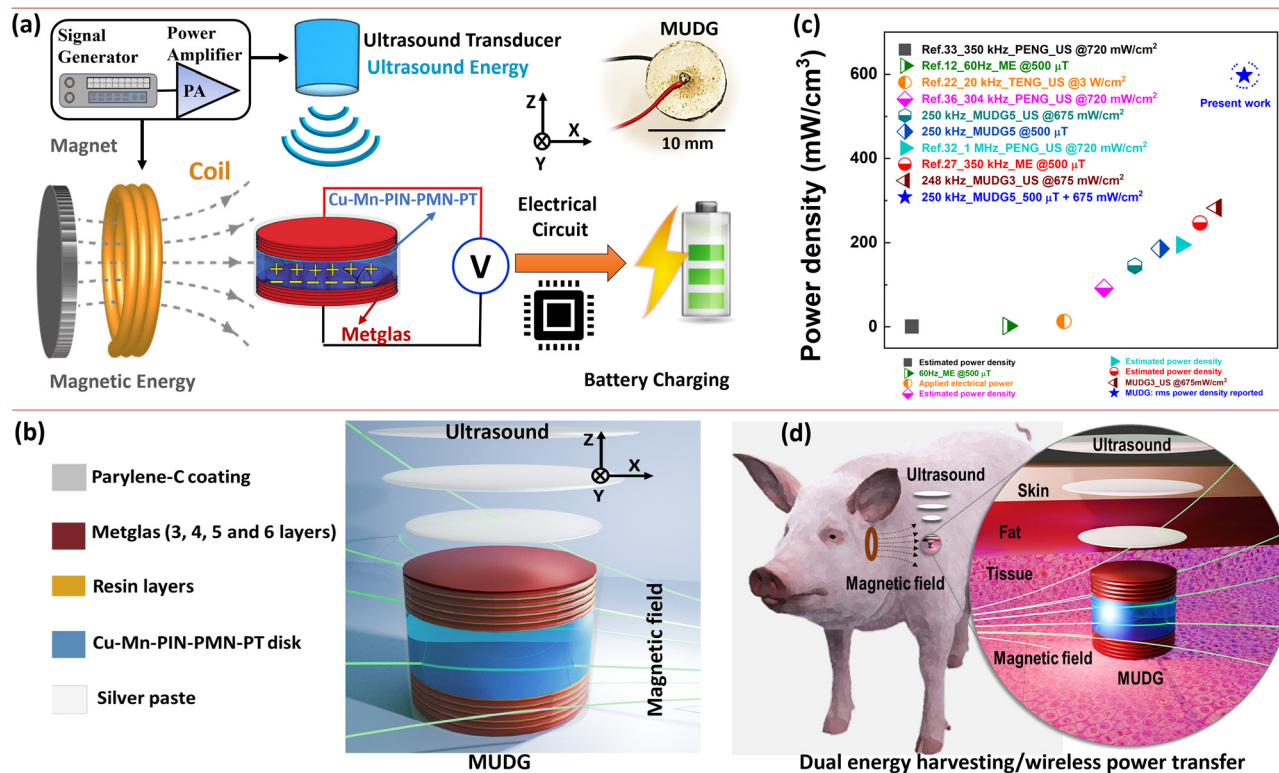
Results and discussion

Magnetic field energy harvesting

The magnetoelectric effect is defined by the generation of electric polarization (P) in a material in response to the applied

2130 | *Energy Environ. Sci.*, 2024, **17**, 2129–2144

This journal is © The Royal Society of Chemistry 2024

Fig. 1 (a) The overview of the present study related to magnetic and ultrasound energy based dual energy harvesting and storage in a battery (inset shows the real image of the MUDG). (b) Schematic representation of the MUDG device for dual (magnetic field and ultrasound) energy harvesting with the description of each component. (c) The comparison of the power density of the MUDG5 device with the other published technologies. (d) For the proof-of-concept experiments, the MUDG is implanted inside the porcine tissue and is wirelessly powered through magnetic field and ultrasound energies simultaneously.

magnetic field (H) (direct effect) or change of magnetization (M) in a material in response to an applied electric field (E) (converse effect) (ESI,† Fig. S3a and b).[37,38] The magnetoelectric device operates through a two-step process for transforming an AC magnetic field into an electric field (direct magnetoelectric effect) or *vice versa*. Initially, the input magnetic field induces a strain (S) in the magnetostrictive layers through magnetostriction. This strain is then transmitted to the piezoelectric layer *via* elastic coupling. Subsequently, mechanical stress (T) emerges in the piezoelectric layer due to elastic stiffness, leading to the creation of surface charge density (D) or polarization through the direct piezoelectric effect. This charge separation results in the generation of an output voltage or electric field within the piezoelectric layer. The magnetic field was applied onto the MUDG devices along its length in the ⟨100⟩ direction of the Metglas sheet and generated output power was measured along the thickness direction (Fig. 2a) in air/water media. Metglas is a better choice to be used as a magnetostrictive layer due to its low cost, lightweight, flexible nature and high saturation magnetostriction at low DC magnetic fields.[12] The deformation in the piezoelectric layer results in the generation of electric charges from the MUDG device through the direct piezoelectric effect. The use of a radial mode disk-shaped piezoelectric layer has an unprecedented advantage for its tolerance to angular misalignment and offers a

higher surface area that is suitable for ultrasound conversion. The amplitude of the ME coupling that is produced by the strain from the magnetostrictive layer is an important factor determining the performance of the MUDG generators. The magnetic energy harvesting performance of the MUDG devices was investigated using a customized 3D-printed Helmholtz coil that generates an AC magnetic field (AC_{Mag}) and DC electromagnets were used for DC magnetic field generation (Fig. 2a). The optimization of magnetostrictive layers has been verified by measuring strain and piezomagnetic coefficient at a constant AC magnetic field and working frequency (ESI† Note S3, Fig. S4–S6 and Table S2). The magnetoelectric voltage coefficient (α_{ME}) is found to be maximized when a specific DC magnetic field is applied along with the AC magnetic field.[21] At a constant frequency, MUDG devices MUDG3, MUDG4, MUDG5, and MUDG6 generate maximum α_{ME} at optimum DC magnetic bias fields of $\sim$190, $\sim$240, $\sim$290, and $\sim$360 Oe ($\sim$15.12, $\sim$19.1, $\sim$23.07 and $\sim$28.65 kA m^{-1}), respectively (Fig. 2b).

The ME coupling relationship for the composites can be written as:[38]

$$\alpha_{ME} = \left| \frac{\partial E}{\partial D} \times \frac{\partial D}{\partial T} \times \frac{\partial T}{\partial S} \right| \times \frac{\partial S}{\partial H} \qquad (1)$$

where E is the electric field, D is the electric displacement, T is

This journal is © The Royal Society of Chemistry 2024

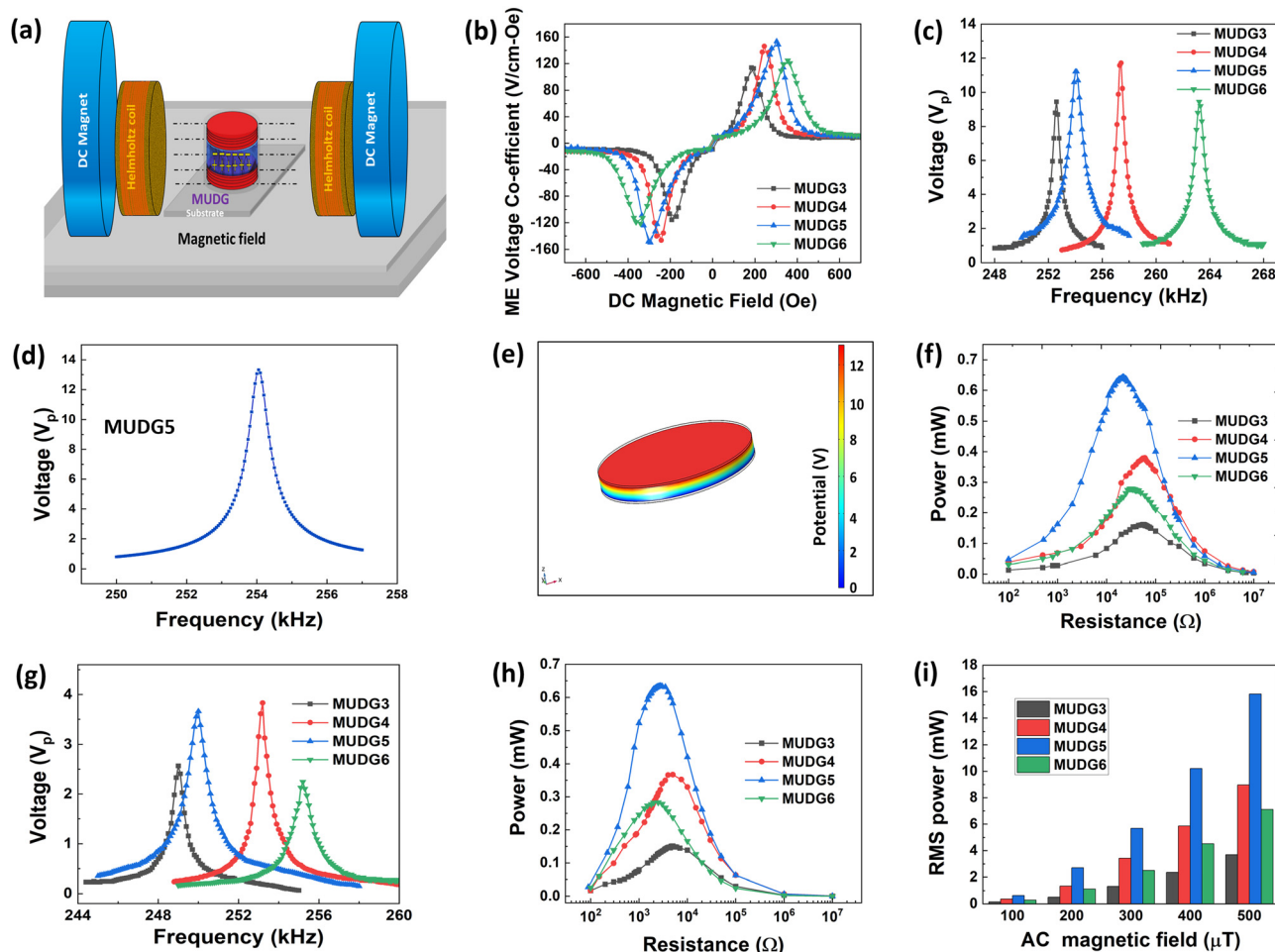*Energy Environ. Sci.*, 2024, **17**, 2129–2144 | **2131**

Fig. 2 (a) Experimental setup of magnetic field energy harvesting is shown schematically. (b) The ME voltage coefficient of MUDG devices as a function of DC magnetic field strength in air medium. (c) The frequency dependent output voltage of the MUDG devices in air medium. (d) Theoretical verification of voltage distribution varying with frequency and (e) piezo-potential distribution in the MUDG5 device at a 100 μT AC magnetic field validated *via* a finite element method. (f) The generated external load dependent output power of the MUDG devices at 100 μT AC magnetic field strength in air medium. (g) The frequency dependent output voltage and (h) output power under the external load of the MUDG devices at a 100 μT AC magnetic field in water medium. (i) The maximum output power generated from MUDG devices at different AC magnetic fields (100–500 μT) in water medium.

the mechanical stress, S is the mechanical strain and H is the magnetic field. The first part of eqn (1) is a non-magnetic factor and hence the modified equation can be written as:

$$\alpha_{ME} \propto \frac{\partial S}{\partial H} = \frac{\partial \lambda}{\partial H} = q \qquad (2)$$

Eqn (2) clearly indicates that the ME response is correlated to the differential of the magnetostriction (λ) and magnetic field values, *i.e.*, directly related to the piezomagnetic coefficients (q). Interestingly, the MUDG5 device exhibited the highest α_{ME} value of $\sim$154 V cm^{-1} Oe^{-1} (1.935 V cm^{-1} A m^{-1}) (Fig. 2b). The combined effect of high strain and piezomagnetic coefficient ($\sim$0.122) resulted in the highest α_{ME} for the MUDG5 device (ESI,† Fig. S4 and S5). Fig. 2c shows the output voltage (V_p) as a function of working frequency of the MUDG devices and the maximum output voltage corresponds to a working frequency range of 252–264 kHz. MUDG5's lower frequency is attributed to a slightly different piezoelectric disk diameter (0.8 mm) compared to the piezo disk (0.78 mm used in

MUDG4). The high voltage for MUDG4 is related to the high impedance of the MUDG4 device (ESI,† Note S4 and Fig. S7). However, the generated power is the highest for the MUDG5 device compared to all MUDG devices as discussed in the following section. The calculated quality factor for MUDG5 is $\sim$290, which has a considerable impact on the link's bandwidth, optimal loading, and importantly power transfer efficiency (ESI,† Note S5, Fig. S8 and Table S3).[21]

To understand the MUDG's output properties under magnetic field, a 3D simulation based on the finite element method (FEM) was analysed using the COMSOL multi-physics software (ESI† Note S6). For simulations to evaluate the magnetoelectric effect, the physics included in the model consisted of solid mechanics, magnetic fields, and electrostatics. A background field with a 100 μT rms AC field and a 250 Oe DC field was set as the magnetic field physics component. The multiphysics of magnetostriction and piezoelectric effects were included. A mechanical damping factor of 0.005 was included for the magnetostrictive and piezoelectric layers. By stationary and

frequency domain perturbation studies, the model was simulated. The frequency dependent output voltage and distribution of piezo-potential within MUDG5 are displayed using a colour code (Fig. 2d and e). The simulated output voltage and frequency dependent behaviour is found to be similar to the experimental results for the MUDG5 device in air medium. However, the experimentally observed voltage is slightly lower ($\sim$12 V) than the simulated result ($\sim$13 V), which could be attributed to the different piezo element and damping factor used in simulation.

The output power of MUDG was measured using external load resistances under a 100 µT AC magnetic field. The optimum load resistance was determined by measuring output voltage while changing the frequency and load resistance, similar to our previous study.[21] The output power was obtained by measuring root-mean-square (rms) output voltage (V_{rms}) at different external load resistances (R_L) (100 Ω to 10 MΩ). The average rms power (P_{rms}) is calculated as follows:[21]

$$P_{rms} = \frac{V_{rms}{}^2}{R_L} \qquad (3)$$

Fig. 2f shows the generated P_{rms} power from MUDG devices under a 100 µT magnetic field at a constant working frequency. The MUDG device achieves an average rms power of 0.66 mW across a load of 22 kΩ at 254 kHz frequency. The MUDG was coated (6–8 µm) with parylene-C due to its biocompatibility, bacterial resistance, chemical resistance, insulation, thickness control and importantly acoustic impedance matching (2.84 Mrayl) close to tissue (1.5 Mrayl). Although PDMS is more transcutaneous, it is difficult to control its thickness and there is high possibility to damage the coating near the soldered area of electrical wires (discussed in detail in the ESI,† Note S7 and Fig. S9a, b).[39,40] To validate any impact on power generation under other external mechanical vibrations, which may arise during body movement, we have measured the output power of the MUDG5 device under a 100 µT magnetic field and with additional applied vibration (frequency: $\sim$1–20 Hz) with 1g acceleration using a commercial shaker (ESI,† Fig. S9c). The results indicate that there is a minimal power degradation ($\sim$0.2–0.3%) generated by the MUDG device (ESI,† Fig. S9d). Hence, we can expect that in a real-world application, with normal body movements the power received by the MUDG device is not affected.

The individual magnetoelectric output performances of the MUDG devices were also checked in water using a 3D printed water tank that fit in between the Helmholtz coils and DC electromagnets (ESI,† Note S8 and Fig. S10). The measured working frequencies of MUDG devices decrease up to $\sim$2–4 kHz under water as compared to in-air operation (Fig. 2g). The lower output voltage for MUDG devices is attributed to the lower impedance in water as compared to air (ESI,† Fig. S7a,b). The power output in water ($\sim$0.65 mW at 2.5 kΩ) is similar to that in air ($\sim$0.66 mW at 22 kΩ) with 1.5% reduction (Fig. 2h). The output voltage is linearly proportional to the AC magnetic field at a constant working frequency (ESI,† Note S8

and Fig. S11a). This suggests a strong potential for achieving high power at high magnetic fields while operating below the safety level i.e. 500 µT AC magnetic field. MUDG5 can generate a high level of power magnitude of $\sim$15.7 mW at 500 µT and 250 kHz frequency. The MUDG5 device shows a high power output due to its superior piezomagnetic constant (ESI,† Fig. S5), enabling it to efficiently transfer maximum strain to the piezoelectric material. MUDG5, thus, represents the optimum device in terms of power performance with the highest magnetoelectric voltage co-efficient/output power under an applied magnetic field (Fig. 2b and i) within the safety limits. Furthermore, the MUDG5 device demonstrates $\sim$4 times the output power of a commercial PZT disk that is 1 mm thick (ESI,† Fig. S11b), which can be attributed to the superior piezoelectric properties of Cu–Mn–PIN–PMN–PT ceramics, including a high-quality factor, good piezoelectric coefficient, and low loss factor. It is noteworthy that the MUDG5 device outperforms other devices reported in the literature in terms of power generation.[24,25,41] It is important to assess the sensitivity of the MUDG device output power to different angular misalignments in different planes under a constant magnetic field for implantable devices. The MUDG5 device can experience angular misalignment in either of the 3 axes – the x-axis or the yz plane; the y-axis or the xz-plane; and the z-axis or the xy-plane (ESI,† Fig. S9g). The measured output power remains independent of angular misalignment (orientation changes) in the xy and yz planes, which is the advantage of our circular-shaped MUDG device (ESI,† Fig. S9e). In contrast, rectangular devices lack such robustness to orientation in the xy plane due to shape anisotropy.[21] For the angular misalignment in the x-axis, no change in the received power is observed as the MUDG device is parallel to the magnetic field lines (ESI,† Fig. S9e). However, for angular misalignment along the y-axis, the power decreases with an increase in the rotation angle from 0 to 90 degrees. In our experimental setup the power drops to $\sim$11 times when the rotation angle changes from 0 to 45 degrees (ESI,† Fig. S9f). To provide robustness in the other scenario, an additional coil can be added in the power transmitter unit to provide two magnetic fields, which are orthogonal (in parallel to the MUDG device surface in all scenarios). Therefore, the proposed MUDG device can truly be robust to any angular misalignment.

Ultrasound energy harvesting

To evaluate the output performance of the MUDG devices, they were subjected to ultrasound pressure using a commercial transducer and output was measured in water to mimic the soft tissue at 5 mm and 15 mm distances (Fig. 3a). Choosing water/tissue media for measuring ultrasound performance is crucial due to their similar acoustic impedance values (1.5/1.7 Mrayl), unlike air (0.0004 Mrayl) with a much higher value, causing a significant reduction in power transfer efficiency.[42,43] The burst mode signal was used to isolate electrical interference and to minimize reflections during the measurements (Fig. 3b). A custom designed 3D printed holder was used to hold the MUDGs/transducers and prevent any misalignment (ESI,† Fig. S12a,b and Note S9). Despite the

This journal is © The Royal Society of Chemistry 2024

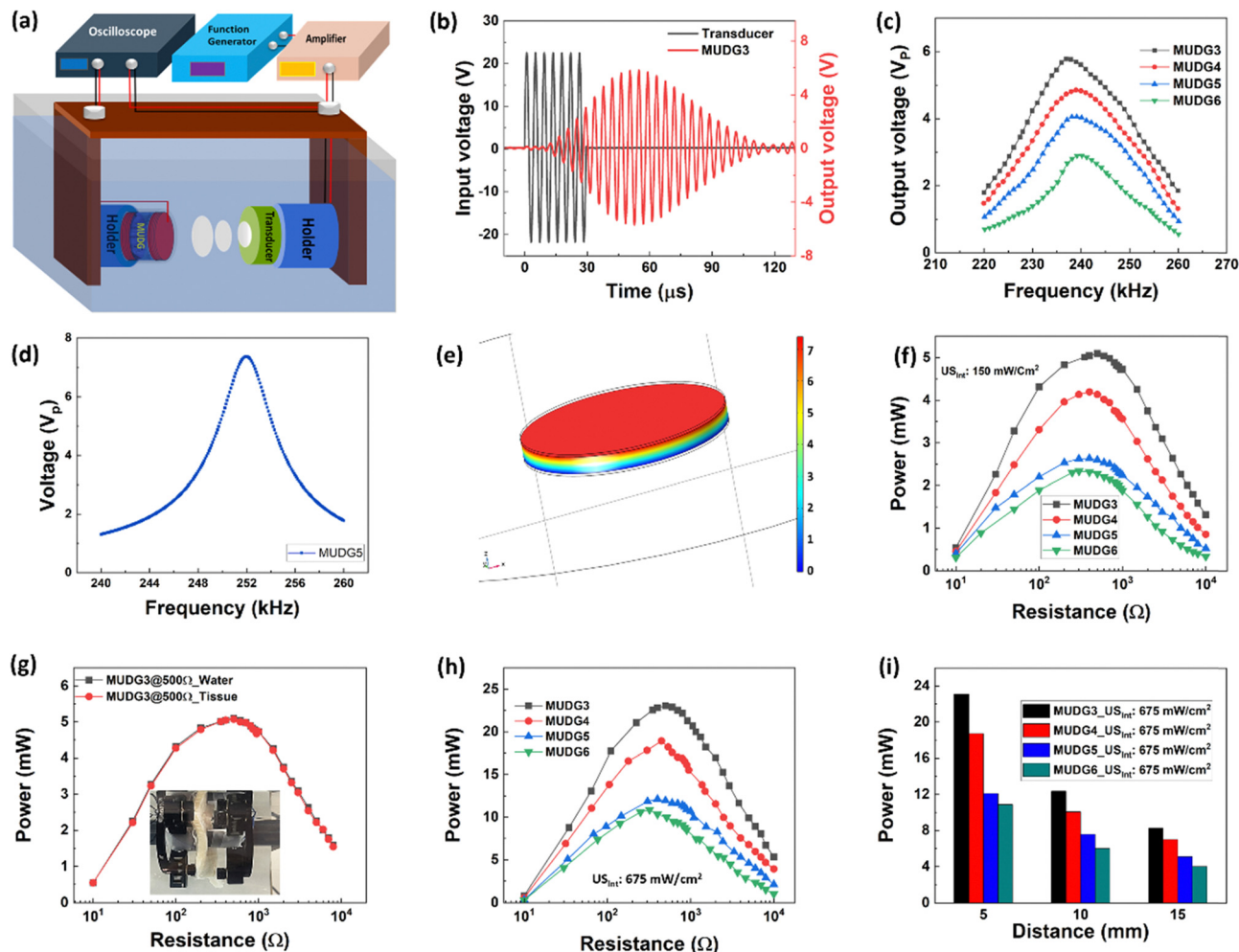*Energy Environ. Sci.*, 2024, **17**, 2129–2144 | **2133**

Fig. 3 (a) The measurement set-up for ultrasound energy harvesting using MUDG devices. (b) The applied input voltage through a commercial transducer and generated output voltage from the MUDG3 device. (c) The frequency dependent output voltage of the MUDG devices during ultrasound energy harvesting. (d) Theoretical validation of output voltage dependent frequency and (e) piezo-potential distribution in the MUDG5 device at 137 mW cm^{-2} ultrasound intensity based on the FEM method. (f) The generated output power was measured by varying external resistance at constant working frequency. (g) Comparison of the output power from the MUDG3 device in water and tissue media. (h) The maximum generated power from MUDG devices at 675 mW cm^{-2}. (i) The output power for MUDG devices at 5, 10 and 15 mm distances.

application of sound pressure on top of the devices, the MUDG devices are capable of vibrating independently in the radial direction at the working frequency under intense ultrasound pressure. The ultrasound transducer was driven at a 45 V$_{p-p}$ applied input voltage. The MUDG devices, powered by the ultrasound energy, were evaluated by measuring their output signals across a broad frequency range of 220–260 kHz (Fig. 3c). The MUDG devices exhibit their maximum output voltage within the frequency range of ∼237–240 kHz, owing to the high input power produced from the transducer in the similar frequency range of ∼237–240 kHz (ESI,† Fig. 12c and d). The MUDG3 device produces a higher voltage output at a 5 mm distance from the transducer compared to other MUDG devices when subjected to a similar ultrasound intensity of ∼150 mW cm^{-2}. This can be attributed to its smaller number of magnetostrictive layers and lower attenuation, and thus higher ultrasound pressure experienced by MUDG3. The

performance at the resonance frequency of the MUDG devices has been verified by adjusting a similar ultrasound intensity level by changing electrical power applied to the transducer, discussed later in the Magnetic field and ultrasound based simultaneous energy harvesting section. To assess the impact of the ultrasound-induced piezoelectric effect, the COMSOL simulations encompassed solid mechanics, transient pressure acoustics, and electrostatics. For this simulation, the airspace was changed to water, and a uniform background pressure field with 10 kPa was applied and the pressure calculated.

The simulation incorporated both acoustic-structure boundary and piezoelectric effect and a 0.008 mechanical damping coefficient was added for magnetostrictive and piezoelectric layers. By frequency domain studies, the model was simulated and the results showed that the frequency dependent output voltage trend was similar to the experimental data (Fig. 3d and e). As expected, the simulated frequency of 252 kHz is closer to

the resonance frequency of 250 kHz for the MUDG5 device and the output voltage is well matched at 250 kHz frequency and at a similar ultrasound intensity.

The rms output power of the MUDG device was measured at a constant ultrasound intensity and frequency across external load resistors. An optimal power of $\sim$5 mW across 500 Ω load was obtained for MUDG3 at a 5 mm distance at 150 mW cm^{-2} ultrasound intensity (Fig. 3f). MUDG5 can generate an output power of $\sim$2.63 mW across 250 Ω load at a 238 kHz working frequency. A larger number of magnetostrictive layers resulted in less output power due to greater pressure attenuation of ultrasound energy transfer resulting in reduced piezoelectric vibration. A linear relationship exists between the input and output voltages of MUDG devices (ESI,† Note S10 and Fig. S13a,b). The output voltage of MUDGs is significantly impacted by the acoustic pressure and acoustic beam area of the transducer. The focal point of a thickness-dependent transducer, which is the beam's minimum width, can be calculated using the following equation:[44]

$$N = \frac{D_0^2 \times f}{4 \times v} \qquad (4)$$

where D_0 is the diameter of the transducer, v is the sound velocity in the medium and f is the working frequency.

The measured approximate focal length of the transducer is $\sim$5 mm and assuming negligible sound loss in the medium, the maximum value of intensity occurs at the focus point. The beam area (30 mm^2) is half of the transducer diameter (i.e., $D_0/2$) used for power generation under ultrasound stimulation but the whole device area is considered for power density calculations. An ex vivo tissue experiment was conducted to confirm the power generation ability of the MUDG devices (Fig. 3g). The tissue power absorption is heavily dependent on the acoustic frequency and penetration depth, as follows:[45]

$$P_{\text{Absorbed}}/P_{\text{Source}} = 1 - e^{-2\alpha_0 f^n d} \qquad (5)$$

where α_0 is the frequency-dependent acoustic absorption coefficient, f is the working frequency and d is the penetration depth. Good acoustic matching of water and tissue with ultrasound decreases the power loss ($\approx$ 0.2%) of the MUDG device.[46] MUDG3 and MUDG5 devices were able to generate $\sim$23.1 mW and 12.2 mW maximum power at 675 mW cm^{-2} intensity at 237 kHz and 238 kHz frequencies, respectively (Fig. 3h). The calculated power transfer efficiency of $\sim$2.1% was achieved for the MUDG3 device. Fig. 3i shows the ability of MUDG3 and MUDG5 devices to generate powers of $\sim$8.28 mW and 5.09 mW at a 15 mm distance, signifying the power transfer capability of these devices under the ultrasound effect. The principle of generation of electricity in piezoelectric material under ultrasound pressure can be explained through the direct piezoelectric effect as shown in ESI,† Fig. S14a,b and Note S10. The mechanical stress (T) deforms the piezoelectric layer, leading to the creation of surface charge density (D) or polarization through the direct piezoelectric effect. This charge separation results in the generation of an output voltage or electric field within the piezoelectric layer.[39] In the MUDG,

under ultrasound pressure, the piezoelectric layer is deformed. This deformation leads to the separation of positive and negative charges, creating an electric dipole and generating a piezopotential. When an external circuit is connected to the deformed piezoelectric material, the flow of current occurs through the external electrodes. During compression, a positive voltage is generated. Under decompression or expansion, the current flows in the opposite direction through the external circuit generating a negative voltage (Fig. S12b).[47]

Magnetic field and ultrasound based simultaneous energy harvesting

To realise the dual energy harvesting capability of MUDG devices under magnetic field and ultrasound stimulation, either individually or concurrently, a continuous sinusoidal mode with infinite cycles was utilized. The experimental setup for measuring dual energy harvesting of MUDG devices is demonstrated in Fig. 4a and ESI,† Note S11, Fig. S15. The schematic illustration of dual energy harvesting in a water medium, where ultrasound is applied perpendicular to the magnetic field, is demonstrated in Fig. 4b. Water was employed as the medium to measure the performance of dual energy harvesting since it has no impact on magnetic fields and has acoustic impedance similar to that of human tissue, particularly for ultrasound.[22]

The magnetoelectric output bandwidth for MUDG devices is lower than that of ultrasound, and below 244 kHz, they do not elicit a response, as shown in Fig. 2g. Hence, resonance frequency related to MUDG devices used for the magnetoelectric effect was selected, such as 250 kHz for MUDG5, and ultrasound intensity was adjusted by changing the electrical power applied to the transducer. Initially, the output voltage of the MUDG5 device was examined to comprehend the combined effect of magnetic field and ultrasound intensity. Under a 200 µT magnetic field, MUDG5 produced an output voltage (V_p) of $\sim$7.29 V, and it generated $\sim$7.14 V under 137 mW cm^{-2} ultrasound intensity (Fig. 4c). Simultaneous measurement confirms the additive output voltage, i.e. $\sim$14.35 V, generated from the MUDG5 device under a 200 µT magnetic field and at 137 mW cm^{-2} ultrasound intensity. MUDG5 exhibits an output power of $\sim$2.65 mW under a 200 µT magnetic field (Fig. 4d) and an output power of $\sim$2.38 mW at 137 mW cm^{-2} ultrasound intensity (Fig. 4e). Fig. 4f shows the resultant output power of MUDGs under simultaneous magnetic field and ultrasound stimulation and under similar measurement conditions. The MUDG5 device shows the maximum output power of $\sim$9.1 mW across 2.5 kΩ load under dual stimulation of magnetic field and ultrasound (Fig. 4e). A similar voltage from both stimulations resulted in 4$\times$ higher power as compared to individual stimulation.

Linear relationships exist between input voltage or AC magnetic field and output voltage in both ultrasound and magnetoelectric measurements, respectively. This is observed for the MUDG5 device, when both AC magnetic field and applied input voltage to the ultrasound transducer are altered (ESI,† Note S12 and Fig. S16a–d). This allows for the
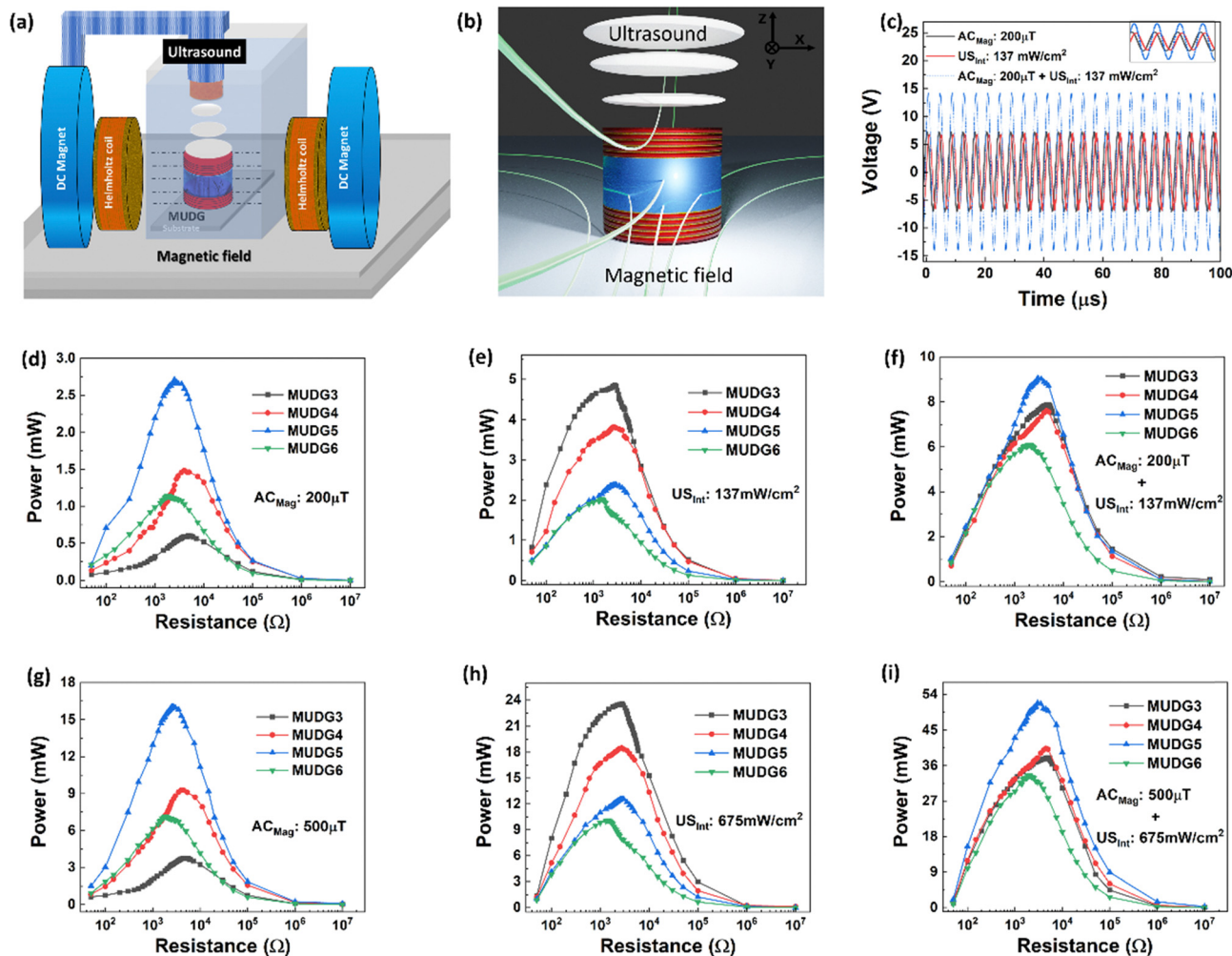
This journal is © The Royal Society of Chemistry 2024

Energy Environ. Sci., 2024, 17, 2129–2144 | 2135

Fig. 4 (a) Measurement set up for a magnetic–ultrasound dual energy harvester and (b) illustration scheme for dual energy harvesting under water. (c) The generated output voltage from the MUDG devices using individual magnetic field/ultrasound and combined (magnetic and ultrasound) technologies (inset shows the zoomed graph). (d) and (e) Generation of output power in MUDG devices varying with external resistance under a 200 μT magnetic field and at 137 mW cm^{-2} ultrasound intensity, respectively. (f) The generated power varying with external load resistance under simultaneous magnetic field and ultrasound energy stimulation. (g) and (h) Generated power variation with external resistance of MUDG devices under a 500 μT magnetic field and at 675 mW cm^{-2} ultrasound intensity, respectively. (i) The generated power variation with external load resistance for MUDG devices under a 500 μT magnetic field and at 675 mW cm^{-2} ultrasound intensity based on simultaneous measurement.

customization of target output power depending on implantable conditions and application areas. The MUDG5 device has the individual power generation ability, that is, ∼15.7 and ∼12.56 mW under a 500 μT magnetic field and at 675 mW cm^{-2} ultrasound intensity (Fig. 4g and h). However, simultaneous stimulation produces an output power of ∼52.1 mW, which is 3× and 4× greater than individual magnetoelectric and ultrasound induced energy harvesting. MUDG5 has the highest power generation ability under a dual energy input *i.e.* at a 500 μT magnetic field and at 675 mW cm^{-2} ultrasound intensity (Fig. 4i). The ultrasound intensity of the transducer was measured using a calibrated hydrophone (details provided in the ESI,† Note S13, Table S4 and Fig. S17a) at working frequencies using the following equation:[48]

$$I = \frac{V_{pp}^2}{8 \times M(f)^2 \times Z} \quad (6)$$

where V_{pp} is the received peak-to-peak voltage across the hydrophone, $M(f)$ is the hydrophone's sensitivity (V/Pa) for a given frequency based on a calibrated data sheet and Z is the acoustic impedance of the water medium. The combined power of ∼52.1 mW harvested is indeed the summation of the voltages, which is close to $\left(\sqrt{15.7} + \sqrt{12.5}\right)^2 = 56.3$ mW. The 8% power loss signifies marginal mismatch of the phases of sign voltage curves under simultaneous measurements (Fig. 4c inset). Despite promising power from individual stimulation, the combined output power under dual stimulation consistently achieves higher power density.

The excellent power transfer efficiency of ∼1.8% was obtained under maximum input power transfer conditions, which was calculated based on the following equation:

$$\eta = \frac{P_{Out}}{P_{Inp}} \times 100\% \quad (7)$$

Assuming a larger beam area of the transducer, which has a similar area to that of the MUDG device, it is expected that the MUDG5 device would be capable of generating >100 mW power with >1.2 W cm^{-3} power density at the point of the human body safety levels (Fig. 1c). Furthermore, evaluating the angular misalignment effects of the MUDG device with respect to the transmitter is important. Misalignments can affect the power received by a receiver device significantly. However, the MUDG has a great advantage due to its geometry and suffers no loss of power with either individual (MF or US) or dual (MF + US) powering when rotated along the z-axis (in xy plane) (ESI,† Fig. S17b). However, it should be noted that rectangular devices face limitations as they cannot simultaneously exploit both advantages. Hence, the results demonstrate that MUDGs can overcome the limitations of conventional wireless power systems for a variety of applications including medical, IoT devices, and structural health monitoring systems, offering a new platform with ultra-high-power capability.

The working mechanism of the MUDG device can be explained by invoking the principle of direct magnetoelectric and piezoelectric effects occurring in different steps under the application of magnetic field and ultrasound, respectively (ESI,† Note S14 and Fig. S18a, b). In the initial stage, when neither magnetic field nor ultrasound is present, the MUDG device does not produce any electrical charge. Subsequently, when a magnetic field is applied, the ME device (which includes a piezoelectric layer) experiences stress and generates electrical charge through the direct magnetoelectric effect, resulting in electricity generation. When ultrasound pressure is additionally applied along with the magnetic field, the ME device experiences even greater stress in the piezoelectric material, leading to the generation of additional electrical charge and, consequently, higher electrical output voltage. As the piezoelectric layers compress under the combined influence of the magnetic field and ultrasound pressure, electrons flow from one electrode to another through an external circuit, causing the ME device to produce a positive signal. Similarly, when the piezoelectric layer expands or decompresses, electrons flow in the opposite direction through the external circuit, generating a negative signal. In the absence of ultrasound and solely under the influence of a magnetic field, the ME device produces a relatively low output voltage due to reduced stress in the piezoelectric layer. Finally, in the absence of ultrasound and magnetic field, the ME device cannot generate any output signal because there is no stress generated in the piezoelectric layer.

Practical applications

The power density of the MUDG device is an important property for practical applications and it can be determined at different input magnetic fields/ultrasound intensities (Fig. 5a). At a lower magnetic field (100 μT) and ultrasound intensity (137 mW cm^{-2}), MUDG3 shows a higher power density due to the predominance of ultrasound over the magnetoelectric effect in comparison to MUDG5 (Fig. 5a). However, MUDG5 can harvest a highest power density of ~596 mW cm^{-2} under simultaneous power transfer conditions when operating closer to the imposed safety limit. To the best of our knowledge, the
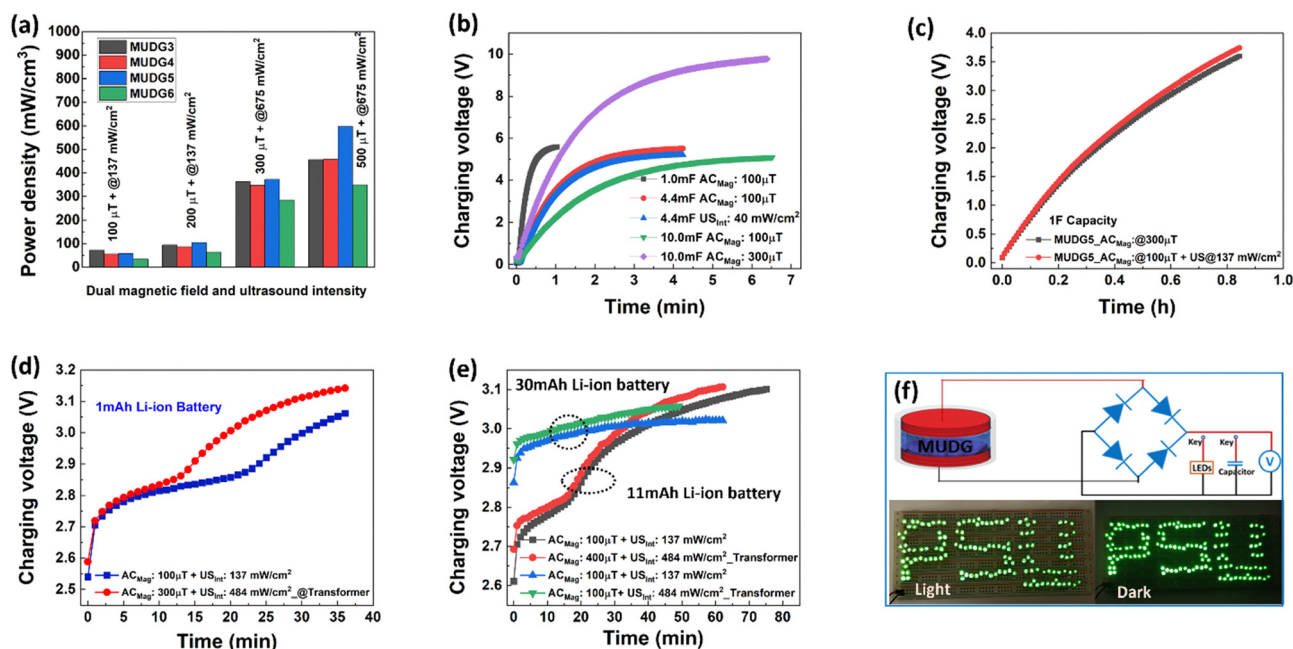

Fig. 5 (a) The average rms power density of the MUDG devices under different magnetic fields and ultrasound intensities. (b) Charging capability of the MUDG5 device for 1, 4.4 and 10 mF capacitors under a 100 μT magnetic field. (c) The charging performance of the MUDG5 device for a 1 F supercapacitor. (d) and (e) The 1, 11 and 30 mA h Li-ion battery charging characteristics using the MUDG5 device under dual magnetic field and ultrasound stimulation with or without the transformer. (f) Demonstration of LED lighting through combination of a bridge rectifier and the MUDG5 device under a 200 μT magnetic field or at 137 mW cm^{-2} ultrasound intensity and the associated circuit diagram.

This journal is © The Royal Society of Chemistry 2024

Energy Environ. Sci., 2024, **17**, 2129–2144 | **2137**

MUDG5 device exhibits the highest power density compared to previously reported devices that employ magnetoelectric, ultrasound, or piezoelectric/triboelectric nanogenerator technologies under comparable conditions (ESI,† Table S5). To demonstrate the practical utility of the MUDG5 device, capacitors, supercapacitors, and batteries were charged by connecting it to a full bridge rectifier to convert the AC to DC electrical signal (ESI,† Fig. S19). The MUDG5 device is capable of rapidly charging capacitors under different conditions. For example, when subjected to a 100 µT magnetic field, the device can charge a 1 mF capacitor to 5.6 V within 1 minute, a 4.4 mF capacitor to 5.5 V within 4 minutes, and a 10 mF capacitor to 5.0 V within 6.5 minutes (Fig. 5b). When exposed to a higher magnetic field of 300 µT, the device can charge a 10 mF capacitor to 9.76 V in 6.36 minutes.

The energy storage (E_{Stored}) ability of the capacitors is calculated as:[49]

$$E_{\text{Stored}} = \frac{1}{2}CV^2 \qquad (8)$$

where C is the capacitance and V is the charging voltage of the capacitor at a definite time (t). MUDG5 is capable of storing high energy up to 15.68 mJ, 66.55 mJ, and 125 mJ for 1 mF, 4.4 mF and 10 mF capacitors within a timeframe of 1 min, 4 min, and 6.5 min under 100 µT AC magnetic field strength (ESI,† Table S6). For a 10 mF capacitor under a 300 µT AC magnetic field strength, MUDG5 can store $\sim$476.29 mJ of energy. The average charging storage power (Pa) that is harvested can be calculated as:[49]

$$P_{\text{a}} = \frac{1}{2}(CV^2 \times 1/t) \qquad (9)$$

where t is the period over which the power is calculated. Based on these measurements, the electrical powers harvested by the MUDG5 device for 4.4 mF and 10 mF capacitors are 0.264 mW and 1.67 mW in 4.2 minutes, which are larger than previously reported results based on an ultrasound energy harvester.[31,49] Hence, the MUDG5 device can charge fast, making it relevant for wireless IoT device's brief timeframes. MUDG5 can charge a 1 F supercapacitor to 3.7 V within 48 minutes at a 300 µT magnetic field and 137 mW cm^{-2} ultrasound intensity. In comparison, a previously reported magnetoelectric device was found to take 275 minutes to charge to 3.7 V under similar measurement conditions (Fig. 5c).[12] The MUDG5 device recharged a commercial Li-ion battery with 1-mAh capacity up to 3.06 V within 36 minutes at a 100 µT magnetic field and 137 mW cm^{-2} ultrasound intensity, with an average charging rate of 1.67 mC s^{-1} (Fig. 5d). In general, the daily power consumption of a commercial pacemaker model KSR701 is around 289 µAh.[22] Thus the MUDG5 device is a safe and efficient option for wirelessly charging pacemaker batteries, neurostimulators, and other IMDs at a faster rate. Recharging at a faster rate is achievable with higher voltage, although the commercial LTC circuit used had a maximum limit on the input voltage of 25 V. Using dual stimulation, the device is capable of charging hig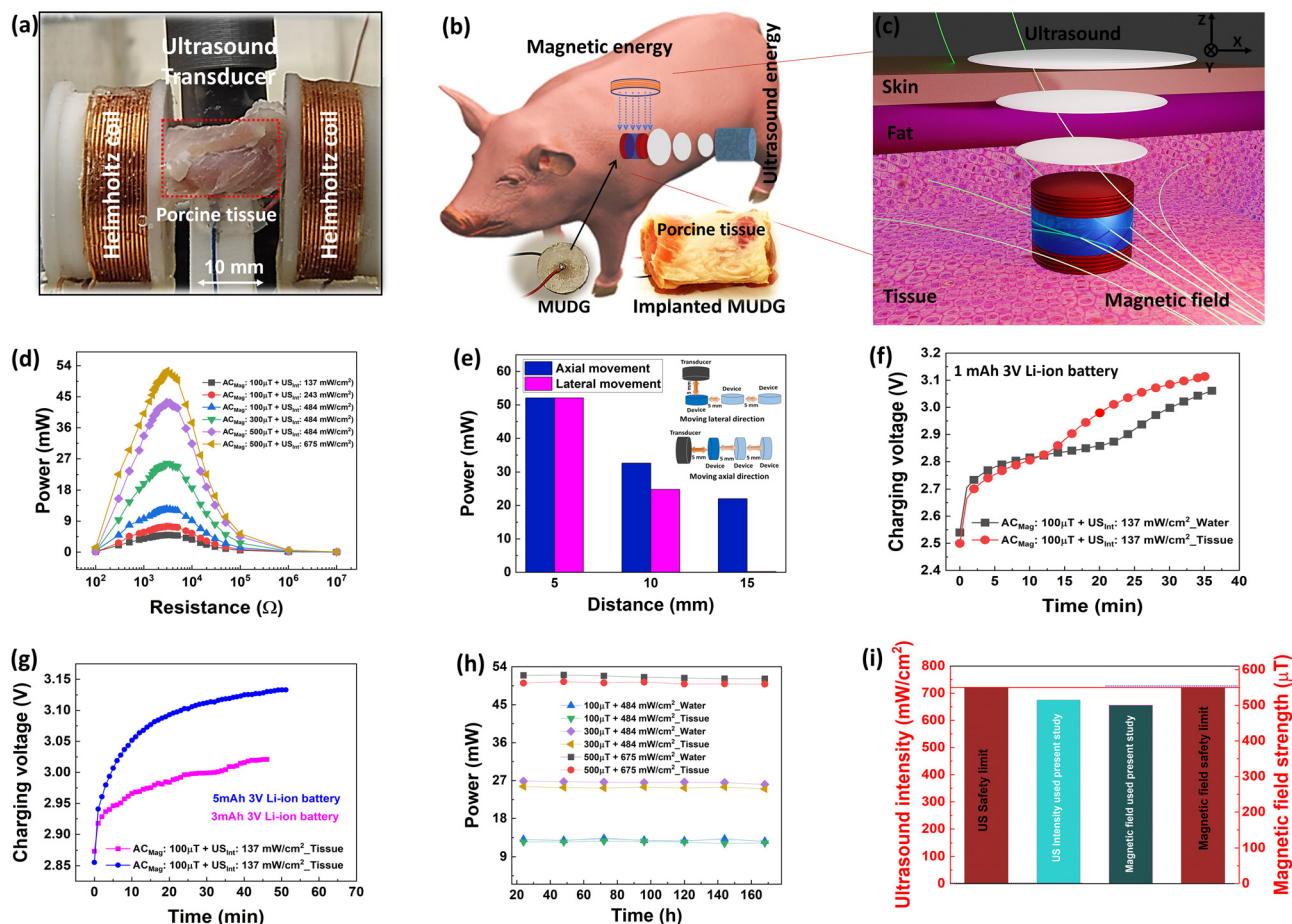h-capacity Li-ion batteries, such as 11 mAh and 30 mAh to 3.1 V in less than an hour, whether a transformer is used or not (Fig. 5e). The detailed information on the battery charging circuit used in the present study is provided in the ESI,† Note S15 and Fig. S20. The MUDG5 device is capable of powering several ($>$130) light-emitting diodes under a 200 µT magnetic field or at 137 mW cm^{-2} ultrasound intensity (Fig. 5f). Hence, the MUDG5 device possesses the potential to energize smart electronics, establishing it as a favorable choice for wirelessly powering IoT devices.

Ex vivo validation

An *ex vivo* study of porcine tissue has been carried out to validate the implantability of MUDG5 as demonstrated for dual energy harvesting under 22 × 40 mm^2 area with different thicknesses (5, 10 and 15 mm) tissue (Fig. 6a–c and ESI,† Note S16, Fig. S21a,b). It is noteworthy that low frequency magnetic fields/ultrasound waves undergo less attenuation in tissue compared to 100s of megahertz and even gigahertz frequencies used by other wireless power transfer modalities such as RF and inductive coupling devices. This absorption greatly reduces an implant's operability, especially at large depths.[21,50,51] Typically, tissues that are 5 and 15 mm in thickness are considered appropriate for implants utilizing wireless energy transfer.[22] The MUDG5 device can generate an high output power of $\sim$52.17 mW in porcine tissue under a 500 µT magnetic field and at 675 mW cm^{-2} ultrasound intensity (Fig. 6d). The output power of the MUDG5 device drops to 22 mW at 15 mm thickness in porcine tissue, primarily due to the device's lower ultrasound pressure and increased damping of tissue that restricts its vibration (Fig. 6e). However, if the transducer is moving in the lateral direction from 5 to 15 mm the energy harvesting performance of MUDG5 is vanished due to misalignment between the transducer and MUDG5. The MUDG5 device can recharge the 1 mAh Li-ion battery up to 3.11 V within 35 min with a 1.78 times faster rate in tissue compared to water (3.06 V within 36 min) (Fig. 6f). The faster charging rate in the tissue medium is attributed to the more concentrating magnetic field strength compared to that in the water medium.[30] The MUDG5 device successfully recharged different batteries with 3 mAh, 5 mAh, 11 mAh and 30 mAh capacities in 5 mm thick porcine tissue (Fig. 6g). The possible capacitive behaviour of Cu wire/insulator/water layers has been removed using Al foils placed in the water near the Helmholtz coils and connected to the ground with the oscilloscope (ESI,† Note S16 and Fig. S21a). It is believed that the performance of the MUDG5 device may be affected under ultrasound due to increased acoustic impedance, attenuation, reflection, and absorption in different tissue interfaces such as fat and muscle. However, the device's performance may be compensated under simultaneous measurement conditions through the induced magnetic field effect. The device has enough stability and durability without losing performance after several hours (160 h) of measurements in water/tissue media under different measurement conditions (Fig. 6h). Parylene-C (PC) is a highly stable and reliable polymer to coat the implantable device for a long term study without damage as stated in an earlier study.[52] We have

2138 | *Energy Environ. Sci.*, 2024, **17**, 2129–2144

This journal is © The Royal Society of Chemistry 2024

Fig. 6 (a) Picture of the implanted MUDG5 device in 5 mm porcine tissue to demonstrate dual energy harvesting. (b) Schematic of the *ex vivo* porcine tissue and the possible location of implanted MUDG5 for implantable device realization. (c) Illustration of dual energy harvesting from MUDG in porcine tissue. (d) Power output of the MUDG5 device under simultaneous energy harvesting varying with external load resistance. (e) Power output of MUDG5 in 5, 10 and 15 mm thick porcine tissue under a 500 μT magnetic field and at 675 mW cm^{-2} ultrasound intensity. (f) and (g) 1 and 3 mA h 3 V Li-ion battery recharging characteristics in water and porcine tissue during simultaneous energy harvesting. (h) The stability of performances of the MUDG5 device measured in tissue for consecutive 170 h. (i) The standard safety level and the measured safety level presented for both magnetic field and ultrasound intensity.

tested the long term durability of the MUDG5 device through measurements for 6 months by operating continuously for 30 min, tested at 1-month intervals (ESI,† Fig. S22). The results predict that the device shows consistent performance with minimal output power reduction (∼3%) (ESI,† Fig. S22). The maximum power was obtained from the MUDG5 device and recharging of different batteries was done under human safety limits as shown in Fig. 6i. Hence, simultaneous utilization of magnetic field and ultrasound for dual energy harvesting presents a distinctive prospect to rapidly recharge batteries. This demonstrates the potential of the MUDG5 device to wirelessly power IMDs such as pacemakers, insulin pumps, neurostimulators, *etc.* It also provides the opportunity to develop power sources for IoT sensors and structural health monitoring sensors.

Cell adhesion and cytotoxicity validation

Typically, parylene-C is a favorable material for encapsulating implantable devices due to its exceptional chemical resistance,

biocompatibility, durability, resistance to bacterial growth, extended shelf life, insulating properties, and, notably, its acoustic impedance, which closely matches that of biological tissue.[52–54] Hence, we conducted experiments using parylene-C-coated samples to evaluate their cytotoxicity through live/dead cell staining and cell viability using MTT assays. Subsequently, we examined Huh7 cell adhesion on various samples, including a control sample coated with poly-L-lysine and parylene-C coated samples both before and after exposure to oxygen plasma treatment for 1 and 5 minutes, over a 24-hour period. In our efforts to promote improved cell adhesion, we applied oxygen plasma treatment to the parylene-C-coated surface for 1 and 5 minutes to enhance the hydrophilic properties of the parylene-C surface, which we confirmed by measuring changes in contact angles (ESI,† Note S17 and Fig. S23). Oxygen plasma treatment is a widely adopted technique to enhance cell adhesion without compromising the material's compatibility and other polymer characteristics.[52,55,56] The results of our experiments revealed that cells adhered to the control sample and to
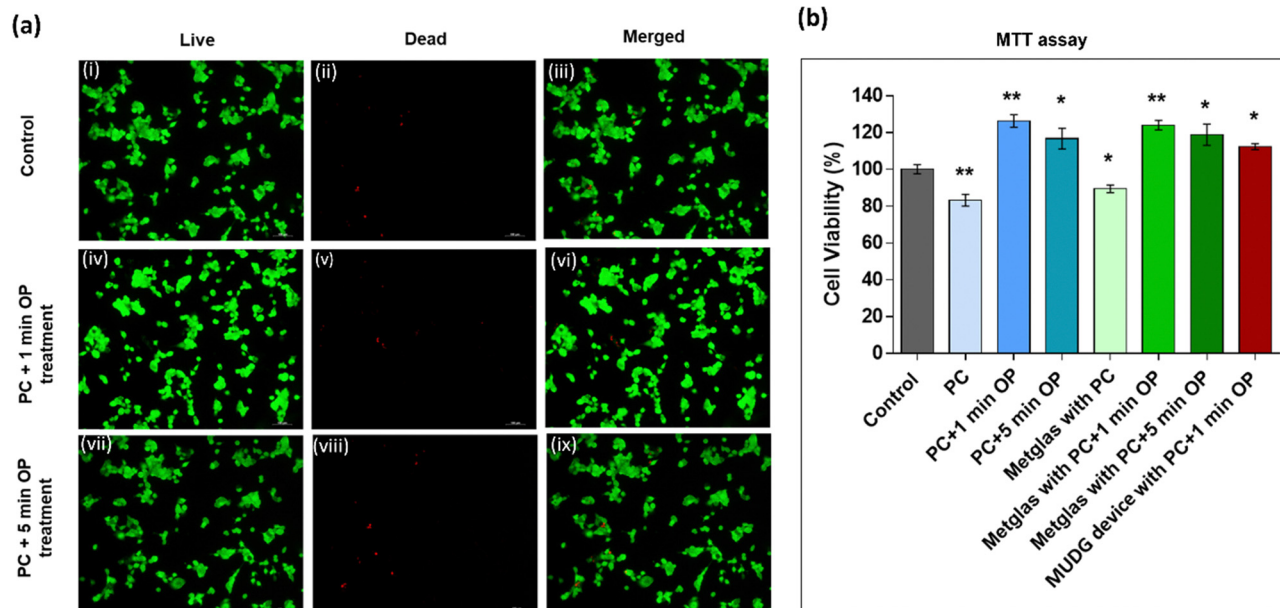
This journal is © The Royal Society of Chemistry 2024

Energy Environ. Sci., 2024, **17**, 2129–2144 | **2139**

Fig. 7 (a) Live/dead staining (green: live cells, red: dead cells). (a(i)–(iii)) Fluorescence images of the control (poly-ʟ-lysine coated coverslips without the PC coating) sample with live, dead and merged views. (a(iv)–(ix)) Fluorescence images of parylene-C coated and oxygen plasma treated (1 and 5 min) samples. Scale bar: 100 μm. (b) Cytotoxicity results of cultured Huh7 cells after 24 h of incubation using parylene-C-coated samples and MTT assay. The statistics was done by comparing all treatments with respect to control. Results are means ± SEM, *$p < 0.05$; **$p < 0.01$. PC: parylene-C, and OP: oxygen plasma.

a slightly lesser extent on the parylene-C coated samples. However, the oxygen plasma-treated samples (1 minute) exhibited an increase in cell adhesion, displaying a uniform distribution likely due to the favourable surface roughness and hydrophilic properties, which are conducive to the growth of live cells (ESI,† Note S18 and Fig. S24a–f).[52] The fluorescence images demonstrated that the control samples (Fig. 7a(i–iii)), which lacked the parylene-C coating, allowed the cells to grow well on the surface with a uniform distribution and limited cell death. In Fig. 7a(iv–ix), the live/dead staining results indicated that the number of live cells on the oxygen plasma-treated parylene-C coated samples (1 and 5 minutes) closely resembled that of the controls. Additionally, there were very few observed dead cells, suggesting minimal cytotoxicity.

The MTT assay results (Fig. 7b) indicate that parylene-C coated samples (coverslips/Metglas/device) exhibited cell viability in the range of ∼85–90% suggesting limited toxicity.[52,56] Similarly oxygen plasma treated parylene-C coated samples exhibited limited toxicity. All these findings suggest that parylene-C-coated samples are non-cytotoxic and support cell viability and that parylene-C-coated MUDG devices have great potential for future biomedical implants.

Safety issue and optimization

We proposed magnetic field and ultrasound assisted dual wireless energy transfer technology *via* designing an architecture that combines a magnetic field initiator, an ultrasonic transducer, and an energy harvester. The reported MUDG5 device was demonstrated to have potential for wireless power transfer applications. Through the understanding of the influence of applied input conditions, such as the magnetic-field

effect on tissue, ultrasound-related biological effects, and compatibility of the devices, further optimization can be conducted to promote the practical utility. In the present study, we have considered the safety limits for AC and DC magnetic field strengths, which are in the range of ≤550 μT and ≤1670 Oe according to the IEEE standard. Hence, the individual and combined technologies have no harmful effects under a 500 μT magnetic field. Under ultrasound energy, some side-effects may occur during the propagation of mechanical waves through organisms, *i.e.*, mechanical, thermal, and other possible effects, if the safety limit is exceeded. This may result in damage to tissue, abnormal cell migration, membrane dysfunction and altered gene expression.[57] As recommended by FDA Track 3, a new set of guidelines published in 1992, the safety limit of the spatial peak temporal average (SPTA) ultrasound intensity is 720 mW cm⁻² for ultrasound diagnostic systems in applications such as peripheral vessel, cardiac, fetal, paediatric, intra-operative, and cephalic imaging.[58] The measured ultrasound intensity for the MUDG5 device is 675 mW cm⁻², which is below the safety threshold and hence no harmful effect occurs at the applied ultrasound intensity. The mechanical index (MI) is an important standard parameter to detect the mechanical damage that usually happens due to the thermal/mechanical effects coming from the side-effects during the propagation of ultrasound waves through organisms. The calculated MI for MUDG5 is 1.3, which is far from the FDA approved safety limit of 1.9 for general ultrasound diagnostic systems. The MI is calculated using the expression:[59]

$$\text{MI} = \frac{P_n}{\sqrt{f}} \times \frac{\sqrt{1\,\text{MHz}}}{1\,\text{MPa}} \tag{10}$$

2140 | *Energy Environ. Sci.*, 2024, **17**, 2129–2144

This journal is © The Royal Society of Chemistry 2024

where f is the centre frequency in MHz and P_n is the peak negative pressure of ultrasound in MPa. Also the possibility to reduce the internal resistance of the devices under high-frequency excitation can increase the power and reduce mechanical damage.[49] The compatibility issue of the fabricated devices is necessary for IMDs. Although the devices are not truly biocompatible, biocompatible parylene C encapsulation can protect the body from biochemical reactions. Parylene C is an FDA approved polymer suitable for encapsulation of IMDs because of several factors *i.e.* biocompatibility, bacterial resistance, chemical resistance, long shelf life, insulation, and importantly its acoustic impedance close to tissue.[52–54] All the above properties of parylene-C can reduce any possible toxic effect and prevent any leaching of particles from the piezoelectric material. We have checked that the parylene-C coated samples even without oxygen plasma treatment have almost no cytotoxicity and have ~ 85–90% cell viability, which indicates their suitability for possible body implantable application although a further study is required for optimization. One can enhance the ultrasound energy harvesting performance by introducing matching impedance among the different layers of the device, which can be calculated using the following equation:[51]

$$Z_M = \sqrt{Z_1 \times Z_2} \qquad (11)$$

where Z_M is the matching impedance layer, and Z_1 and Z_2 are the acoustic impedance layers of the 1 and 2 materials, respectively.

The present work demonstrates a high-power small-scale energy harvesting device, which can harvest ultrasound and magnetic field simultaneously. In the future, wireless signal actuation/transmission chips can be integrated into this wireless energy transfer system to realise diverse uses and functions for IMDs for healthcare monitoring and data communication.

Conclusion

A novel dual energy harvesting technology using magnetic field and ultrasound-driven wireless energy transfer has been introduced to convert magnetic/acoustic energy into electricity using a millimeter-scale energy harvesting device, adding a new dimension to millimeter-scale electronics/IMDs. This work investigated dual technology based on magnetic field and ultrasound power in liquids and soft tissues. The capability for wireless power transfer through water and porcine tissue media was successfully demonstrated. Following FDA and IEEE regulations, the fabricated MUDG5 device can generate a stable high output power of ~ 52.1 mW and allow an *ex vivo* study of porcine tissue within the human safety limit for the magnetic field and ultrasound intensity. The prototypes can generate power on the order of milliwatts, enabling charging of capacitors and supercapacitors; and recharging of a 1 mAh capacity Li-ion battery at a rate of ~ 1.67 mC s^{-1} in porcine tissue within 30 min. This enables the capability to power IMDs such as pacemakers, implantable cardioverters, insulin pumps, *etc.*

Furthermore, the parylene-C coated MUDG device has excellent cell viability (85–90%) with limited cytotoxicity and is promising for biomedical implants. We note that future improvements can include exploring the integration of acoustic components, high-performance piezoactive elements, and wireless information transmission and actuation chips to create efficient, safe, controllable, and communicable wireless systems.

Methods

Fabrication of MUDG devices

To fabricate the MUDG devices, a piezoelectric disk (made in our lab, ESI,† Note S1) was sandwiched between the magnetostrictive layers. The magnetostrictive layers (2605SA, Metglas) were attached on the piezoelectric disk using epoxy (DP-460, 3M) to form a layered composite. In order to ensure the connectivity between the magnetostrictive layers with the piezoelectric disk (on either side), silver paste (Leitsilber 200 Silver Paint, Ted Pella) was used. The excess overspill was removed by hand polishing the sides with 1200/P4000 grit sandpaper, followed by basic testing of the transducer and finally coating it with ~ 6–8 μm biocompatible parylene-C using the vapor deposition method. To acquire the output power from the MUDG device, electric wires were soldered on both sides of the device. The fabrication procedures of the devices are provided in detail in ESI,† Note S2 and Fig. S2. Based on FEM analysis using the COMSOL Multiphysics software (details provided in the ESI,† Note S6), the measured data have been verified considering the properties of PZT4 as a piezoelectric layer and Metglas as a magnetostrictive layer.

Parylene-C coating

Parylene C films were fabricated by the Chemical Vapor Deposition (CVD) method using a PDS 2010 LABCOTER, at the Millennium Science Complex, Penn State University, PA, USA. The process involved utilizing a dimer of chloro-*para*-xylylene as a precursor, which was heated to 680 °C, causing it to decompose into its monomeric form. These monomers were then deposited and polymerized spontaneously in the vapor phase at room temperature under a pressure of 10^{-3} mbar. The coating thickness can be regulated by adjusting the deposition time.

Oxygen plasma treatment

In order to functionalize the parylene C surface to make it more hydrophilic, the oxygen plasma treatment was carried out using a Tepla M4L at 50 W and a pressure of 500 mTorr. The varied parameter was the time of exposure to the plasma, for 1 and 5 min.

Contact angle measurement

The contact angle is the angle formed when a drop of liquid comes into contact with a solid surface. To understand the hydrophobic/hydrophilic characteristics of the parylene-C coated MUDG device before and after treatment with oxygen

This journal is © The Royal Society of Chemistry 2024

Energy Environ. Sci., 2024, **17**, 2129–2144 | **2141**

plasma (1 and 5 min), the contact angle was measured using a goniometer (ramé-hart) with a minimum of 5 measurements per sample.

Cell culture

To study the cytotoxicity of the packaging materials, Huh7, the human hepatoma cell line, was used as an *in vitro* model. The cell line was maintained in DMEM (Dulbecco's Modified Eagle Medium, Life Technologies) with high glucose and L-glutamine supplemented with 10% fetal bovine serum (Atlanta Biologicals) and 1% penicillin–streptomycin (Life Technologies) in a humidified tissue culture incubator at 37 °C and in a 5% CO_2 atmosphere. The Huh7 cells were cultured on coverslips coated with poly-L-lysine (Neuvitro).

Cytotoxicity assay

Huh7 cells were cultured in 24-well plates with coverslips coated with poly-L-lysine (control), coverslips coated with parylene-C before or after oxygen plasma treatment (1 min and 5 min), parylene-C coated Metglas before or after oxygen plasma treatment (1 min and 5 min) and a parylene-C coated metal device with 1 min oxygen plasma treatment for 24 h. The MTT assay kit (Abcam) was used to measure the percentage cell viability according to the manufacturer's instructions. The absorbance of the negative control (cells without the parylene-C coating or oxygen plasma treatment) is 100%. The percentage of growth inhibition is calculated as: cell viability (%) = (absorbance of experimental wells/absorbance of control wells) × 100. The experiment was performed in triplicates.

To evaluate cell viability, Huh7 cells were cultured on poly-L-lysine coated glass coverslips with or without the parylene-C coating followed by oxygen plasma treatment for 1 min and 5 min. After 24 h, cell viability was assessed by using the LIVE/DEAD Viability/Cytotoxicity Kit (Molecular Probes). For this assay the cells were cultured in a 24 well plate. The medium was removed, and the cells were washed twice in phosphate buffered saline (PBS). Cells were incubated with assay reagents containing 2 µM calcein AM (green-fluorescence labeled live cells) and 4 µM ethidium homodimer-1 (red-fluorescence labeled dead cells) for 45 minutes at room temperature. The live and dead cell images were captured on a Nikon ECLIPES 50i microscope with the NIS Elements imaging software (Melville, NY).

Statistical analysis

Graph Pad Prism 9.1.1 version software (GraphPad, San Diego, CA) was used to analyze the data. Statistics was done with one-way analysis of variance (ANOVA) for multiple data sets, followed by Tukey's multiple comparison test. Results are expressed as means ± SEM. A p value of 0.05 or less was considered statistically significant.

Characterization

A Helmholtz coil controlled by a function generator was used as an AC magnetic field source. The MUDG devices were placed at the center of the circular structure of the coil to apply homogeneous magnetic fields to the device. To apply accurate amplitudes of AC magnetic fields, the AC magnetic fields were calculated based on the number of turns in the coil, and the magnitude was confirmed by measuring the AC magnetic fields using a Gauss meter. The open-circuit voltage was measured using an oscilloscope (Keysight DSO1014A) under various AC and DC magnetic field strengths. The impedance of the MUDG devices in an air/aqueous medium was measured using a network analyzer (E5071C, Tektronix, USA). To calculate the average rms power, the rms voltage was measured across a variable resistor ranging from 50 Ω to 10 MΩ. The power density was calculated by dividing the average power by the entire volume of the MUDG devices including, the Perylene-C coating. To measure optimum DC bias and ME voltage coefficients of the MUDG devices, an electromagnet (GMW Magnet System, Model: 3472-70) was employed to supply DC magnetic fields, while the Helmholtz coil supplies the AC magnetic field at working frequency. The ME voltage co-efficient was measured in the range of −700 to700 µT DC magnetic field using a lock-in amplifier (SR830, Stanford Research Systems). The strain value of the Metglas layers was measured using a strain gauge (Micro-Measurements) with the help of a P3 strain indicator and recorder. To explore the practical utility of the device, commercial green LEDs were powered and furthermore capacitors and supercapacitors were charged using the generated power from the MUDG devices. A bridge rectifier (MB1S-TP, Micro Commercial Co.), which enables AC–DC conversion, was used for LED lighting and capacitor charging. The different coin cell Li-ion 3 V battery (Seiko Instruments and Panasonic) with different capacities (1, 3, 5, 11 and 30 mAh) were successfully charged through an appropriate charging circuit (ESI,† Fig. S20) using the MUDG5 device under different input power conditions. SMA connectors and ground shields have been used in the whole study to avoid outside electrical interferences.

Author contributions

2142 | *Energy Environ. Sci.*, 2024, **17**, 2129–2144

This journal is © The Royal Society of Chemistry 2024

and S. P. revised the final manuscript. M. K. and S. P. supervised the project. All authors contributed to the discussions and revision of the manuscript.

Conflicts of interest

The authors declare no competing interests.

Acknowledgements

References

1 J. Rinne, J. Keskinen, P. R. Berger, D. Lupo and M. Valkama, *IEEE Access*, 2017, **5**, 27868–27878.

2 T. Sanislav, S. Zeadally, G. D. Mois and S. C. Folea, *J. Network Comput. Appl.*, 2018, **121**, 149–158.

3 Y. Chen, Y. Cheng, Y. Jie, X. Cao, N. Wang and Z. L. Wang, *Energy Environ. Sci.*, 2019, **12**, 2678–2684.

4 R. J. Vullers, R. Van Schaijk, H. J. Visser, J. Penders and C. Van Hoof, *IEEE Solid-State Circuits Mag.*, 2010, **2**, 29–38.

5 Z. Chu, Z. Sun, B. Wang, K. Song, J. Wang, J. Gao and S. Dong, *Adv. Energy Mater.*, 2022, **12**, 2103345.

6 C. Jiang, X. Li, S. W. M. Lian, Y. Ying, J. S. Ho and J. Ping, *ACS Nano*, 2021, **15**, 9328–9354.

7 S. Roundy, D. Steingart, L. Frechette, P. Wright and J. Rabaey, Wireless Sensor Networks: First European Workshop, Proceedings 1, 2004, vol. 2920, pp. 1–17.

8 M. A. Wood and K. A. Ellenbogen, *Circulation*, 2002, **105**, 2136–2138.

9 M. Piñuela, P. D. Mitcheson and S. Lucyszyn, *IEEE Trans. Microwave Theory Tech.*, 2013, **61**, 2715–2726.

10 N. Wang, L. Han, H. He, N.-H. Park and K. Koumoto, *Energy Environ. Sci.*, 2011, **4**, 3676–3679.

11 J. Chun, H.-C. Song, M.-G. Kang, H. B. Kang, R. A. Kishore and S. Priya, *Sci. Rep.*, 2017, **7**, 41383.

12 H. Lee, R. Sriramdas, P. Kumar, M. Sanghadasa, M. G. Kang and S. Priya, *Energy Environ. Sci.*, 2020, **13**, 1462–1472.

13 P. Basset, S. P. Beeby, C. Bowen, Z. J. Chew, A. Delbani, R. Dharmasena, B. Dudem, F. R. Fan, D. Galayko and H. Guo, *APL Mater.*, 2022, 10.

14 S. K. Karan, R. Bera, S. Paria, A. K. Das, S. Maiti, A. Maitra and B. B. Khatua, *Adv. Energy Mater.*, 2016, **6**, 1601016.

15 S. K. Karan, S. Maiti, J. H. Lee, Y. K. Mishra, B. B. Khatua and J. K. Kim, *Adv. Funct. Mater.*, 2020, **30**, 2004446.

16 G. T. Hwang, V. Annapureddy, J. H. Han, D. J. Joe, C. Baek, D. Y. Park, D. H. Kim, J. H. Park, C. K. Jeong and K. I. Park, *Adv. Energy Mater.*, 2016, **6**, 1600237.

17 M. Peddigari, J. H. Park, J. H. Han, C. K. Jeong, J. Jang, Y. Min, J.-W. Kim, C.-W. Ahn, J.-J. Choi and B.-D. Hahn, *ACS Energy Lett.*, 2021, **6**, 1383–1391.

18 S. R. Khan, S. K. Pavuluri, G. Cummins and M. P. Desmulliez, *Sensors*, 2020, **20**, 3487.

19 C.-L. Su, C.-C. Cheng, P.-H. Yen, J.-X. Huang, Y.-J. Ting and P.-H. Chiang, *Commun. Biol.*, 2022, **5**, 1166.

20 A. Ibrahim and M. Kiani, *IEEE Trans. Biomed. Circuits Syst.*, 2016, **10**, 1100–1111.

21 S. Hosur, R. Sriramdas, S. K. Karan, N. Liu, S. Priya and M. Kiani, *IEEE Trans. Biomed. Circuits Syst.*, 2021, **15**, 1079–1092.

22 R. Hinchet, H.-J. Yoon, H. Ryu, M.-K. Kim, E.-K. Choi, D.-S. Kim and S.-W. Kim, *Science*, 2019, **365**, 491–494.

23 V. Annapureddy, M. Kim, H. Palneedi, H. Y. Lee, S. Y. Choi, W. H. Yoon, D. S. Park, J. J. Choi, B. D. Hahn and C. W. Ahn, *Adv. Energy Mater.*, 2016, **6**, 1601244.

24 J. Ryu, J.-E. Kang, Y. Zhou, S.-Y. Choi, W.-H. Yoon, D.-S. Park, J.-J. Choi, B.-D. Hahn, C.-W. Ahn and J.-W. Kim, *Energy Environ. Sci.*, 2015, **8**, 2402–2408.

25 V. Annapureddy, S.-M. Na, G.-T. Hwang, M. G. Kang, R. Sriramdas, H. Palneedi, W.-H. Yoon, B.-D. Hahn, J.-W. Kim and C.-W. Ahn, *Energy Environ. Sci.*, 2018, **11**, 818–829.

26 C. Chen, Z. Wen, J. Shi, X. Jian, P. Li, J. T. Yeow and X. Sun, *Nat. Commun.*, 2020, **11**, 1–9.

27 J. C. Chen, P. Kan, Z. Yu, F. Alrashdan, R. Garcia, A. Singer, C. Lai, B. Avants, S. Crosby and Z. Li, *Nat. Biomed. Eng.*, 2022, **6**, 1–11.

28 Z. Yu, J. C. Chen, Y. He, F. T. Alrashdan, B. W. Avants, A. Singer, J. T. Robinson and K. Yang, *IEEE J. Solid-State Circuits*, 2021.

29 Z. Yu, J. C. Chen, B. W. Avants, Y. He, A. Singer, J. T. Robinson and K. Yang, *IEEE Int. Solid-State Circuits Conf.*, 2020, 510–512.

30 Z. Yu, J. C. Chen, F. T. Alrashdan, B. W. Avants, Y. He, A. Singer, J. T. Robinson and K. Yang, *IEEE Trans. Biomed. Circuits Syst.*, 2020, **14**, 1241–1252.

31 Q. Shi, T. Wang and C. Lee, *Sci. Rep.*, 2016, **6**, 1–10.

32 T. Zhang, H. Liang, Z. Wang, C. Qiu, Y. B. Peng, X. Zhu, J. Li, X. Ge, J. Xu and X. Huang, *Sci. Adv.*, 2022, **8**, eabk0159.

33 L. Jiang, Y. Yang, R. Chen, G. Lu, R. Li, D. Li, M. S. Humayun, K. K. Shung, J. Zhu and Y. Chen, *Nano Energy*, 2019, **56**, 216–224.

34 D.-M. Lee, N. Rubab, I. Hyun, W. Kang, Y.-J. Kim, M. Kang, B. O. Choi and S.-W. Kim, *Sci. Adv.*, 2022, **8**, eabl8423.

35 W. F. Pritchard Jr and R. F. Carey, *Radiology*, 1997, **205**, 27–36.

36 L. Jiang, Y. Yang, R. Chen, G. Lu, R. Li, J. Xing, K. K. Shung, M. S. Humayun, J. Zhu and Y. Chen, *Adv. Funct. Mater.*, 2019, **29**, 1902522.

37 K.-H. Cho and S. Priya, *Appl. Phys. Lett.*, 2011, 98.

38 Y. Zhou, D. J. Apo and S. Priya, *Appl. Phys. Lett.*, 2013, **103**, 192909.

This journal is © The Royal Society of Chemistry 2024

Energy Environ. Sci., 2024, **17**, 2129–2144 | **2143**

39 X. Zhuang, A. Nikoozadeh, M. Beasley, G. Yaralioglu, B. Khuri-Yakub and B. Pruitt, *J. Micromech. Microeng.*, 2007, **17**, 994.

40 S. Hosur, S. K. Karan, S. Priya and M. Kiani, *IEEE Biomed. Circuits Syst. Conf.*, 2022, 6–10.

41 K.-W. Lim, M. Peddigari, C. H. Park, H. Y. Lee, Y. Min, J.-W. Kim, C.-W. Ahn, J.-J. Choi, B.-D. Hahn and J.-H. Choi, *Energy Environ. Sci.*, 2019, **12**, 666–674.

42 K. Kobayashi, S. Yoshida, Y. Saijo and N. Hozumi, *Ultrasonics*, 2014, **54**, 1922–1928.

43 S. Hughes, *Phys. Educ.*, 2001, **36**, 468.

44 M. Meng and M. Kiani, *IEEE Trans. Biomed. Circuits Syst.*, 2016, **11**, 98–107.

45 D. Christensen, *Ultrasonic Bioinstrumentation*, John Wiley & Sons Incorporated, 1988.

46 L. E. Houston, A. O. Odibo and G. A. Macones, *Prenatal Diagn.*, 2009, **29**, 1204–1212.

47 L. Jiang, Y. Yang, Y. Chen and Q. Zhou, *Nano Energy*, 2020, **77**, 105131.

48 S. Hosseini, K. Laursen, A. Rashidi, T. Mondal, B. Corbett and F. Moradi, *IEEE Trans. Ultrason. Eng.*, 2020, **68**, 191–200.

49 L. Jiang, G. Lu, Y. Yang, Y. Zeng, Y. Sun, R. Li, M. S. Humayun, Y. Chen and Q. Zhou, *Energy Environ. Sci.*, 2021, **14**, 1490–1505.

50 H. Dinis and P. Mendes, *Biosens. Bioelectron.*, 2021, **172**, 112781.

51 H. S. Gougheri, A. Dangi, S.-R. Kothapalli and M. Kiani, *IEEE Trans. Biomed. Circuits Syst.*, 2019, **13**, 835–847.

52 M. Golda-Cepa, K. Engvall, M. Hakkarainen and A. Kotarba, *Prog. Org. Coat.*, 2020, **140**, 105493.

53 J.-M. Hsu, L. Rieth, R. A. Normann, P. Tathireddy and F. Solzbacher, *IEEE Trans. Biomed. Eng.*, 2008, **56**, 23–29.

54 G. E. Loeb, M. Bak, M. Salcman and E. Schmidt, *IEEE Trans. Biomed. Eng.*, 1977, **2**, 121–128.

55 H. R. Holmes, E. L. Tan, K. G. Ong and R. M. Rajachar, *Biosensors*, 2012, **2**, 57–69.

56 S.-J. Kim, D.-S. Lee, I.-G. Kim, D.-W. Sohn, J.-Y. Park, B.-K. Choi and S.-W. Kim, *Kaohsiung J. Med. Sci.*, 2012, **28**, 123–129.

57 H. Shankar, P. S. Pagel and D. S. Warner, *J. Am. Soc. Anesthesiol.*, 2011, **115**, 1109–1124.

58 Department of Food and Administration, *Guidance for Industry and FDA Staff*, 2008.

59 T. L. Szabo, *Diagnostic Ultrasound Imaging: Inside Out*, Academic press, 2004.

2144 | *Energy Environ. Sci.*, 2024, **17**, 2129–2144

This journal is © The Royal Society of Chemistry 2024